Nanofocus x-ray diffraction and cathodoluminescence investigations into individual core–shell (In,Ga)N/GaN rod light-emitting diodes

Thilo Krause[1], Michael Hanke[1,4], Zongzhe Cheng[1], Michael Niehle[1],
Achim Trampert[1], Martin Rosenthal[2], Manfred Burghammer[2],
Johannes Ledig[3], Jana Hartmann[3], Hao Zhou[3],
Hergo-Heinrich Wehmann[3] and Andreas Waag[3]

[1] Paul-Drude-Institut für Festkörperelektronik, Hausvogteiplatz 5–7, D-10117 Berlin, Germany
[2] European Synchrotron Radiation Facility, BP 220, F-38043 Grenoble Cedex, France
[3] Institute of Semiconductor Technology, Braunschweig University of Technology, Hans-Sommer-Straße 66, D-38106 Braunschweig, Germany

E-mail: krause@pdi-berlin.de and hanke@pdi-berlin.de

Abstract

Employing nanofocus x-ray diffraction, we investigate the local strain field induced by a five-fold (In,Ga)N multi-quantum well embedded into a GaN micro-rod in core–shell geometry. Due to an x-ray beam width of only 150 nm in diameter, we are able to distinguish between individual m-facets and to detect a significant in-plane strain gradient along the rod height. This gradient translates to a red-shift in the emitted wavelength revealed by spatially resolved cathodoluminescence measurements. We interpret the result in terms of numerically derived in-plane strain using the finite element method and subsequent kinematic scattering simulations which show that the driving parameter for this effect is an increasing indium content towards the rod tip.

Keywords: x-ray diffraction, III-V semiconductors, nanowires and nanorods, finite element method

1. Introduction

The three-dimensional (3D) growth of low-dimensional semiconductors such as nanowires or rods has triggered an increasing interest in research and industry over the last few years due to a plethora of potential applications. Alongside to single-photon emission [1–3] and solid-state lightning [4–7], various other applications are being pursued [8–11]. The increased surface-to-volume ratio offers an efficient way of achieving elastic strain relaxation and, thus, the possibility of combining highly lattice-mismatched material compounds in a pseudomorphically strained alloy. Moreover, the 3D device design, e.g. in a core-shell geometry, offers a drastic increase in the active area compared to conventional planar films [12–14]. Consequently, these objects are discussed as the next generation of low-cost, high-efficiency light-emitting diodes (LEDs).

Especially interesting are $In_xGa_{1-x}N$-based devices where the incorporation of In from $x = 0$ to 1 allows one to tune the emitted wavelength over the full optical spectrum [15]. However, up to now, a major drawback of rod-like structures was that the efficiency of conventional planar structures has not been reached yet. Reasons for this might be, on the one hand, the growth regimes for low-dimensional structures which are usually different to the ones used for conventional structures [16]. On the other hand, the

---

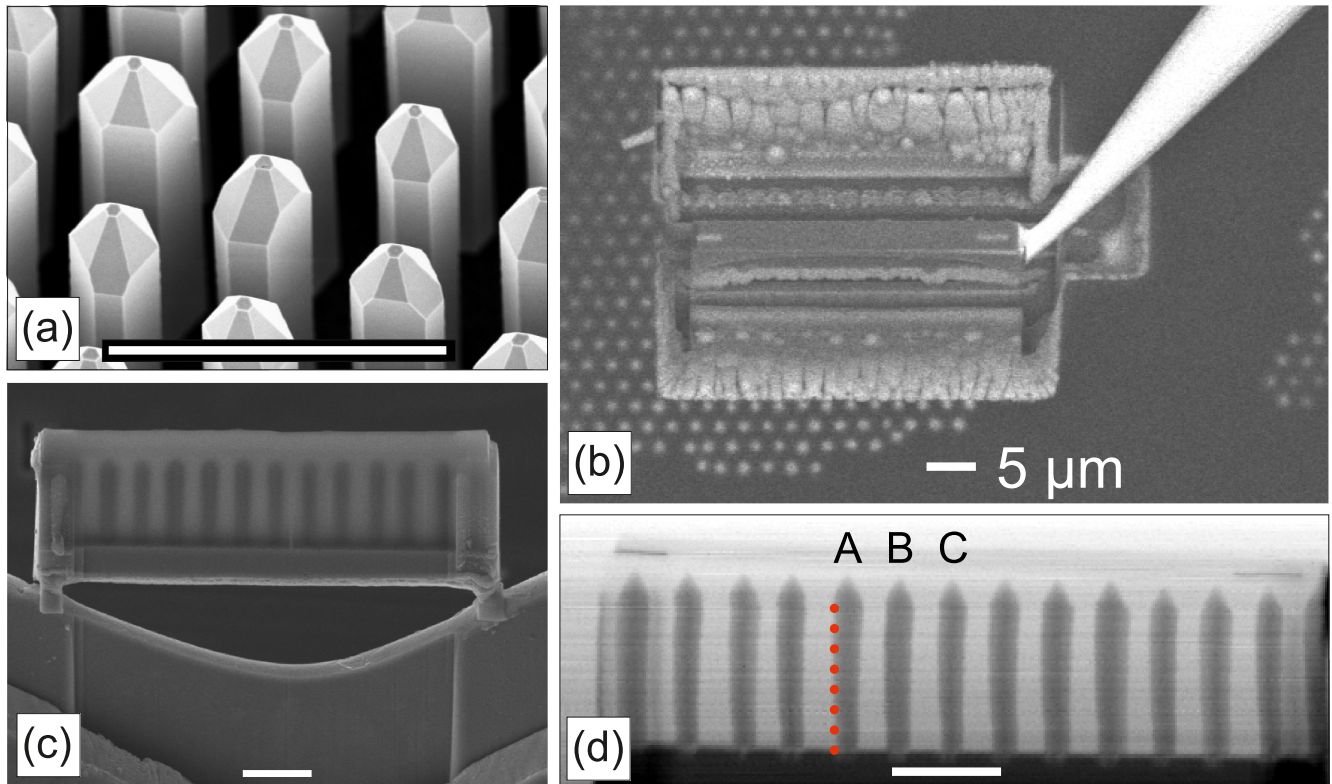[4] Author to whom any correspondence should be addressed.

Figure 1. Bird's-eye view scanning electron micrograph recorded under a tilt of 30° for the (In,Ga)N/GaN micro-rods as-grown (a). Next to the lamella, trenches are visible as well as the manipulator needle used for lifting out (b). Scanning electron micrograph of the embedded sample mounted on a support (c), and scanning x-ray transmission image of the extracted lamella containing a single row of free-standing rods recorded with 150×150 nm^2 spot size (d). Red dots indicate vertical sampling positions (cf figure 4(a)). The horizontal white scale bars refer to 5 μm in all images.

characterization necessary for improvement increases in complexity with decreasing homogeneity within an ensemble of low-dimensional objects. In fact, it becomes necessary to obtain information about individual objects to draw conclusions about the overall constitution of the ensemble and its optoelectronic performance. However, important properties for the device performance such as morphology, chemical composition and the resulting strain state of different individual objects cannot be analyzed conveniently with standard characterization techniques as they lack either resolution or are time-consuming. Here, nanofocus x-ray diffraction with a resolution in the sub-μm regime, available at synchrotron sources, has proven to be a powerful technique [17–20]. In scanning nanofocus x-ray diffraction experiments, information about the strain state can be related to the comparatively high spatial resolution of the x-ray beam [21–23]. Recently, a 2D strain-mapping scheme was even presented which will allow the investigation of micro-rod ensembles with reference to individual rods [24]. Moreover, as nanofocus x-ray diffraction is a non-destructive technique, the correlation of the strain state in individual objects to, for example, electrical properties [25] is possible.

In this study we investigate the in-plane strain field for the example of three neighboring core-shell (In,Ga)N/GaN rods using nanofocus x-ray diffraction. The strain state in individual facets of the rods is analyzed and correlated to

representative spatially resolved cathodoluminescence (CL) measurements. We interpret the results employing the numerical finite element method and subsequent kinematic scattering simulations.

2. (In,Ga)N/GaN core-shell rods

2.1. Growth

The (In,Ga)N/GaN micro-rods shown in figure 1 are grown by selective area metalorganic vapor phase epitaxy (MOVPE) on a GaN buffer layer on a Al$_2$O$_3$ substrate. A SiO$_x$ mask was deposited on top and structured with holes 800 nm in diameter and with a pitch of 2.4 μm. In this way, the rods with a hexagonal cross-section of 1 μm in diameter and a height of 8 μm grow at pre-defined and well-ordered positions (see figure 1(a)). For the growth of the n-doped GaN core, trimethylgallium, NH$_3$ and SiH$_4$ were injected into the vertical close-coupled showerhead reactor. With the help of a low V/III ratio (33) and high SiH$_4$ flows (110 nmol min^{-1} in the first half of the growth, 16 nmol min^{-1} thereafter), vertical growth was favored [26]. Following the core growth, the shell layers of the LED structures were grown under standard layer conditions with high V/III ratios. First, an unintentionally doped GaN shell was deposited. Following this, a five-fold (In,Ga)N/GaN multi-quantum well (MQW) containing

3 nm-thick barriers and wells with an estimated QW real temperature of 700 °C and a 70 nm-thick Mg-doped p-GaN shell was grown. Through *in situ* annealing under a H₂-free atmosphere, the p-GaN was activated.

2.2. Focused ion beam sample preparation

In order to obtain information about individual rods, we used a Ga⁺ focused ion beam (FIB) to isolate a single row of neighboring, free-standing rods within a lamella. Here, FIB is an ideal preparation technique as it allows a targeted isolation of low-dimensional objects with the additional freedom of choosing its crystallographic orientation within a lamella [27]. For the FIB preparation, the rods were embedded by epoxy glue diluted with acetone to reduce the viscosity. For conductivity enhancement, the glue was mixed with carbon black. The embedded rods were protected by a carbon depot with which the first and last rod of the lamella were also marked. Figure 1(b) shows a scanning electron micrograph (SEM) of the lamella with trenches next to it. Using a manipulator needle, the lamella was lifted out and mounted on a standard copper grid, as shown in figure 1(c). Using small beam sizes, fine polishing steps were performed to get rid of the re-deposited GaN crystallites. Due to the short penetration depth into the glue, Ga atoms were not implemented into the rods themselves such that the active regions were still functioning. The orientation of the rods within the lamella was chosen in such a way that an m-plane faces its neighboring m-plane such that we can access the in-plane strain in the $\langle 10\bar{1}0 \rangle$ direction. Depending on the particular position on the rod we can distinguish between Bragg and Laue cases.

3. Results and discussions

3.1. Nanofocus x-ray diffraction experiments

Probing strain at the sub-μm scale with hard x-rays remains a domain of synchrotron-based, highly specialized experimental stations. Here, we used a setup at beamline ID13, located at the European Synchrotron Radiation Facility (ESRF), which consists of silicon-based nanofocusing compound refractive lenses (CRL) [28] and realized a spot size of 150×150 nm² FWHM with a photon flux of about 10^7 photons/second at 14.9 keV. All diffraction patterns were recorded by an Eiger 4M detector. We initially aligned the lamella using an optical microscope and further improved its adjustment by scanning x-ray transmission. The latter technique was used to picture the lamella investigated, shown in figure 1(d).

To access the in-plane strain normal to the m-facets, as sketched in figure 2(a), we have probed the $\{10\bar{1}0\}$ lattice planes using the example of three neighboring individual rods labeled A, B and C in figure 1(d). We performed horizontal scans over all these rods with a step size of 100 nm and repeated the series at eight different heights such that we covered the range from bottom to tip, as indicated by the red

spots in the same figure. At each position, we recorded angle-resolved maps to retrieve information about the strain induced by the MQW by measuring the separation of GaN and (In,Ga)N-related peaks. Figure 2(c) shows a representative excerpt of the measured reciprocal space maps (RSMs) retrieved from rod A at its highest position in figure 1(d), which is just below the pyramid-shaped top of the rod. In the RSM, the peak separation along the radial direction (q_{rad}) contains information about the strain state whereas the angular direction (q_{ang}) is strain-insensitive and mainly influenced by the shape function of the rod (cf figure 2(b)).

As sketched in figure 2(a) the indices E1 to E7 refer to a horizontal movement of the x-ray probe across the object. Between position E1 and E3 the beam mainly illuminates the vicinity close to the $(10\bar{1}0)$ m-facet and, in particular, the embedded MQW. In contrast, at the central location E4, areas near the symmetry axis, exclusively, are probed and eventually, from E5 to E7, the effective scattering volume approaches the opposite MQW near the $(\bar{1}010)$ facet. All RSMs contain a contribution at the nominal position for relaxed GaN at $q_{rad} = 2.277$ Å⁻¹. However, at smaller q_{rad}, a pronounced peak related to (In,Ga)N is only detected at positions E1 and E7 and loses intensity while the beam moves towards the rod center. At position E4, where the x-ray beam hits the symmetry axis, the contribution completely vanishes.

This can be understood by looking at the in-plane strain map (see figure 3) as simulated by the finite element method (FEM) using the commercial package MSC Marc®. Here, we see the ε_{xx} component of the *total* strain tensor [29] which takes relaxed GaN as a reference. It it worth noting that total strain and peak positions in reciprocal space, with respect to a substrate reference, are directly related. In the simulation, we assume a constant QW thickness of 3 nm and an In content of 10%. The elastic constants are taken from [30], while for the ternary (In,Ga)N alloy they were obtained via linear interpolation following Vegard's law. It is noteworthy that the inherent six-fold symmetry of the problem is virtually reduced (to a two-fold symmetry) as soon as it is plotted in Cartesian coordinates. However, if the incident plane wave is diffracted on the $\{10\bar{1}0\}$ lattice planes, i.e. along the *x*-axis, ε_{xx} directly maps the strain component to which the x-ray beam is sensitive.

In orthogonal coordinates, the two opposing m-facets parallel to the *y*-axis have zero contribution in ε_{yy} (not shown) such that ε_{xx} is maximal. The surface normals of the four m-facets in between are a superposition of the *x*- and *y*-direction, resulting in non-zero ε_{xx} and ε_{yy} components, which likewise yield smaller values for ε_{xx} as is visible in figure 3. Comparing the in-plane strain map with the volume illuminated by the x-ray beam (cf figure 2(a)) indicates that at position E1 the MQW in the $(10\bar{1}0)$-facet is covered—an area where ε_{xx} approaches its maximum. At position E4, however, the x-ray beam illuminates a volume where ε_{xx} is considerably smaller. That is why the separation between the GaN and (In,Ga)N peak decreases and cannot be resolved anymore. When reaching the opposing facet at E7, ε_{xx} becomes maximal again while ε_{yy} vanishes. Hence, the (In,Ga)N peak
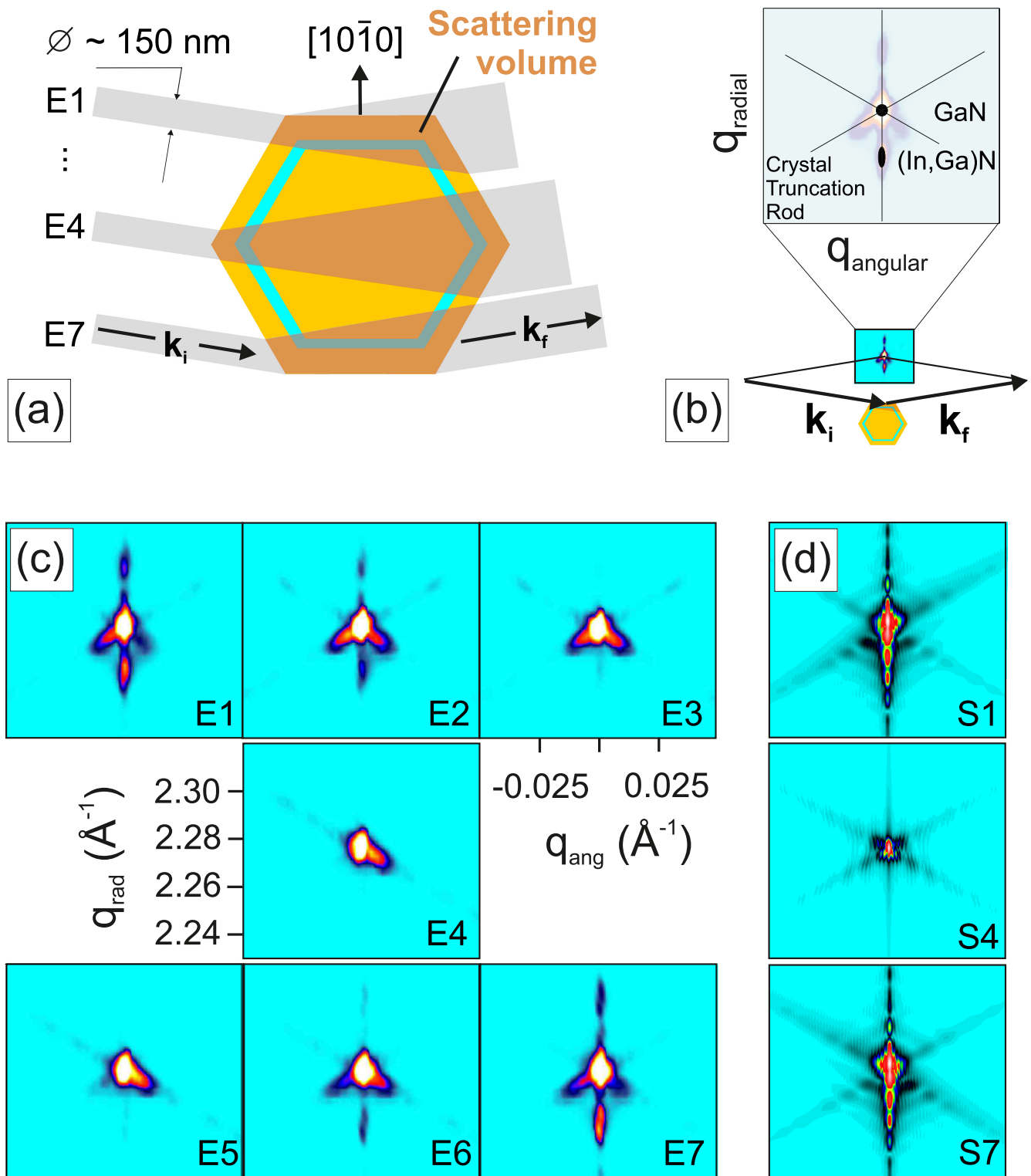
Figure 2. Sketch of the scattering volume at different beam positions on the rod (a). Here, $\mathbf{k}_i$ and $\mathbf{k}_f$ depict the wave vectors of incident and diffracted x-ray beams with a connecting scattering vector perpendicular to an m-plane, thus along $[10\bar{1}0]$. In the symmetric diffraction regime the reciprocal space is probed along the radial, here the $[10\bar{1}0]$ direction. In this way the length of the scattering vector $|\mathbf{q}| = |\mathbf{k}_f - \mathbf{k}_i|$ changes and due to different lattice parameters one may expect a separation of GaN and (In,Ga)N-related contributions (b). However, the (orthogonal) angular direction will be probed as long as $|\mathbf{q}| = $ constant. This section of reciprocal space mainly contains information from the rod shape since it is insensitive to strain. (c) Shows experimental reciprocal space maps at different horizontal positions corresponding to sketch (a). The similarity between pattern E1 and E7 indicates that both opposing facets are equivalent in terms of in-plane strain, while a missing (In,Ga)N contribution at the central position E4 hints at an unstrained area in the middle of the rod. (d) Depicts simulated scattering patterns using equation (2) where positions S1, S4, S7 correspond to positions E1, E4, E7.
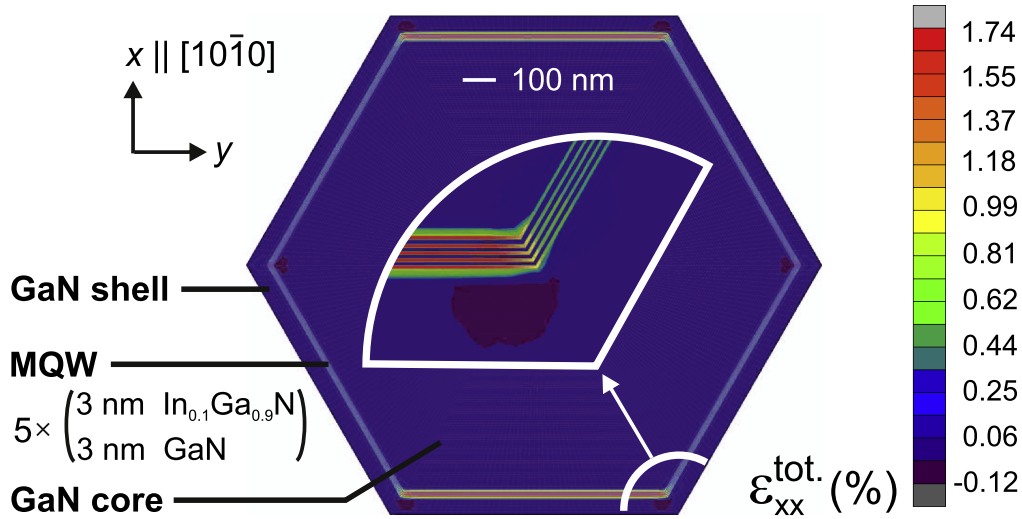
Figure 3. Total strain component ε_{xx} as derived by the finite element method, assuming an embedded symmetric five-fold GaN/(In,Ga)N MQW containing 10% In and a quantum well thickness of 3 nm.

reappears. This indicates that the resolution of the x-ray beam allows it to distinguish the strain field in individual facets.

To confirm this interpretation, we performed kinematic scattering simulations based on the displacement field obtained by FEM. In the limit of weak photon scattering, which is justified for low-dimensional structures, the kinematic scattering approach is particularly powerful for simulating three-dimensional intensity patterns of diffusely scattered x-rays [31, 32]. In order to mimic the situation of the nanofocus x-ray diffraction experiment performed, we appended a Gaussian beam profile

$$G(\mu, \sigma) \equiv \frac{1}{\sqrt{2\pi}\,\sigma} \exp\left[-\frac{(r_i - \mu)^2}{2\sigma^2} \right] \qquad (1)$$

to the kinematic sum

$$I(\boldsymbol{q}) \propto \left| \sum_i G(\mu, \sigma) f_i(\boldsymbol{q}) \exp\left[i\boldsymbol{q} \cdot (\boldsymbol{r}_i + \boldsymbol{u}(\boldsymbol{r}_i)) \right] \right|^2 \qquad (2)$$

which enables us to position the beam center with μ and to tune the FWHM, which is related to the variance σ via $\sigma = \text{FWHM}/2\sqrt{2ln(2)}$. In the kinematic sum $\boldsymbol{q} = (q_x, q_y, q_z)$ denotes the reciprocal lattice vector, $f_i(\boldsymbol{q})$ is the atomic form factor, and $\boldsymbol{r}_i$ points towards the individual atoms. The atomic displacement $\boldsymbol{u}(\boldsymbol{r}_i)$ is retrieved via interpolation of the atomic coordinates $\boldsymbol{r}_i$ with the displacement field $\boldsymbol{u}$ obtained from FEM. We note that the scattering process becomes rather complex when dealing with a highly collimated and hence divergent beam profile which is, as such, not perfectly approximated by a plane wave scenario. Only a fraction of the experimental 150 nm-wide x-ray spot carries a divergence small enough to excite scattering, which in turn favors features in even smaller areas (in our case the length scale of the MQW). On the other hand, the Gaussian profile of a simulated plane wave fulfills the Bragg condition in every spot and, therefore, the (larger) volume of the 70 nm-thick GaN shell becomes prominent.

Figure 2(d) shows three simulated RSMs based on equation (2) matching positions E1 (S1), E4 (S4) and E7 (S7) of figure 2(c). The assumed In content of 10% equals the envisaged, nominal composition. At S1 and S7 we can clearly see the modulation of the x-ray diffraction pattern due to elastic strain caused by the MQW. It is this modulation which vanishes in S4, where the beam is positioned in the rod center. The good agreement between experiment and simulations allows us to conclude that this modulation is actually sensitive to the very local in-plane strain induced by a MQW in a single facet. Moreover it indicates that the MQW is coherently strained. Further evidence of the beam position on the rod is the appearance and disappearance of crystal truncation rods (CTRs), which can be related to the illuminated facets [33]. All six CTRs only become visible if the beam illuminates three facets (cf S1 and S7).

By moving the x-ray beam vertically along the rod we are able to detect changes of the in-plane strain in a vertical direction. Figure 4(a) shows line profiles of the scattered intensity along [10$\bar{1}$0], which is the strain sensitive q_{rad} direction. The line profiles were extracted from experimental RSMs taken at eight different heights in steps of 1 μm on the left facet of rod A (as indicated by the red spots in figure 1(d)). As expected, a peak at the q_{rad} value for relaxed GaN is visible at all line profiles. However, for the bottom 3 μm we cannot detect any (In,Ga)N-related contribution. Beyond this level only a weak fingerprint, just below the GaN peak, appears and shifts to smaller q_{rad} values with increasing scanning height. This behavior was well reproduced for all investigated facets of rods A, B and C.

In order to find the origin of the shift in the in-plane strain field, we simulated the dependency of the peak position on the In content as well as on the QW thickness using equation (2). Transmission electron microscopy analysis yields a QW width of around (3 ± 1) nm, which we found to have a weak influence on the diffraction pattern and the (In,Ga)N peak position (not shown). Moreover, FEM simulations confirm that a QW thickness variation in the order of
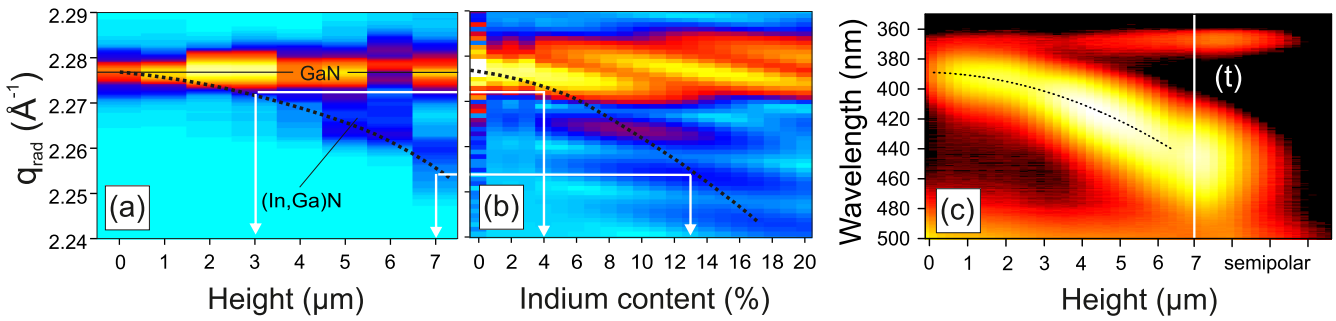
Figure 4. (a) Sequence of line profiles along q_{rad} ($q_{ang} = 0$) extracted from measured RSMs at the positions indicated by the red spots in figure 1(d). Simulated line profiles along the same direction for different In contents ranging from 0 to 20% (b) and the sequence of CL spectra (line scan) while exiting along a representative individual micro-rod with a sidewall facet of 7 μm height (c). The dashed black lines are a guide to the eye indicating the position of the (In,Ga)N-related peak with respect to the rod height (a) and the In content (b). In (c) the dashed line is a quadratic fit on the peak wavelength of the QW emission versus the rod height (c). The line (t) marks the onset of the top region. The (In,Ga)N peak positions at different heights in (a) can be directly translated (via solid white arrow lines) into different In contents (b). Please note that (a) and (b) are composite figures, which consist of individual line scans in a radial scan direction.

1 nm changes the maximum value of ε_{xx} only by a very small amount (0.002%), thus approaching the planar case at the facet center. However, a change of the chemical composition, indeed, has a strong impact on the (In,Ga)N peak position as the subsequent replacement of Ga by In atoms directly increases the lattice mismatch with the surrounding GaN matrix. This correlation can be seen in the simulated line profiles shown in figure 4(b). Here, the scattered intensity is plotted as a function of the In content and q_{rad}. The beam position on the rod was chosen such that the maximum of the beam profile is placed in the middle of the MQW embedded close to the $(10\bar{1}0)$-facet, corresponding to position E1 in figure 2(c). The GaN contribution stays at a constant q_{rad} value, however, as soon as the five-fold (In,Ga)N MQW is considered the GaN peak smears out due to interference effects. Moreover, the (In,Ga)N peak, appearing below the GaN bulk contribution, bends towards smaller q_{rad} values with increasing In content. As a guide to the eyes, the dashed line in figure 4(b) follows the maximum of the (In,Ga)N-related peak. The modulation along q_{rad} (for a fixed In content) is due to the shape function matching the periodicity of the outer p-type GaN shell of about 70 nm thickness. On the basis of the kinematic scattering simulations shown in figure 4(b) we can conclude that the In content x in the In$_x$Ga$_{1-x}$N MQW changes from about 4 ± 1 to 13 ± 1% over a height of 4 μm. A possible scenario to explain this effect is related to the high density of rods, which induces a diffusion gradient in the gas phase during the MQW growth. The particular three-dimensional morphology including tall rods, separated by narrow, μm-deep and empty volumes, causes a vertical non-homogeneity in a way that the carrier gas can preferentially deliver more In at elevated areas of the rods. As a direct consequence, the gas flow approaching their very bottom becomes substantially depleted of In, which in turn yields a smaller incorporated amount.

3.2. Spatially resolved cathodoluminescence

The gradient in the In content along the rod height has a significant impact on the optical performance of the LED. In their wurtzite modification the two binaries GaN and InN have direct bandgaps of about 3.4 and 1.8 eV. Following Vegard's law, which connects these two limits in a linear fashion, will yield a subsequently smaller band gap with increasing In content. In figure 4(c) we show representative cathodoluminescence (CL) spectra from a line scan along a single rod obtained at a substrate tilt of 30° by exciting small regions of about 0.01 μm^2 with an electron probe of 15 keV and about 170 pA. At a wavelength of 365 nm the near-band-edge luminescence from GaN is visible. In the bottom region of the rod, the MQW emits at a wavelength of 390 nm. Above a height of approximately 3 μm the emitted wavelength is gradually red-shifted to larger wavelengths up to 440 nm at the top of the sidewall. Due to the orientation-dependent growth mechanism, the In incorporation on the r-planes at the rod tip proceeds in a different fashion compared to the side-facets. Here, a higher In content is observed as well as a smaller QW width. This results in an emission at even higher wavelength, here at about 450 nm. At a wavelength of about 500 nm, yellow luminescence resulting from point defects inside the GaN matrix can be observed [34]. The overall trend shown in figure 4(c) was observed for all individual LED rods investigated at different positions on the wafer and agrees very well with the investigation of the in-plane strain field measured by nanofocus x-ray diffraction.

4. Conclusion

We presented a spatially resolved investigation of individual core-shell (In,Ga)N/GaN micro-rods using nanofocus x-ray diffraction. Due to the aspect ratio of about 1:10 of the spot size and rod diameter, and an even better resolution along the rod height, we were able to analyze the in-plane strain field within individual facets and to detect a significant strain gradient in the MQW along the rod height. With supporting finite element simulations and subsequent kinematic scatter-ing simulations we were able to identify a gradient in the In content along the rod height as the origin of this in-plane strain gradient. We complemented the in-plane strain analysis

with spatially resolved CL measurements showing that the strain gradient can be directly correlated to a significant red-shift of the MQW emission along the rod height. Our results show that the sub-μm resolution available at the synchrotron sources provides an ideal technique to locally analyze μm-sized individual objects. In fact, this resolution is ideal to measure the local strain state even within individual facets of a single rod in its as-grown environment, while methods with, for example, higher atomistic resolution or with lower penetration depth would fail.

Acknowledgments

References

[1] Claudon J, Bleuse J, Malik N S, Bazin M, Jaffrennou P, Gregersen N, Sauvan C, Lalanne P and Gerard J-M 2010 A highly efficient single-photon source based on a quantum dot in a photonic nanowire *Nat. Photonics* **4** 174–7

[2] Reimer M E, Bulgarini G, Akopian N, Hocevar M, Bavinck M B, Verheijen M A, Bakkers Erik P A M, Kouwenhoven L P and Zwiller V 2012 Bright single-photon sources in bottom-up tailored nanowires *Nat. Commun.* **3** 737

[3] Holmes M J, Choi K, Kako S, Arita M and Arakawa Y 2014 Room-temperature triggered single photon emission from a III-nitride site-controlled nanowire quantum dot *Nano Lett.* **14** 982–6

[4] Qian F, Gradečak S, Li Y, Wen C-Y and Lieber C M 2005 Core/multishell nanowire heterostructures as multicolor, high-efficiency light-emitting diodes *Nano Lett.* **5** 2287–91

[5] Kishino K, Kikuchi A, Sekiguchi H and Ishizawa S 2007 InGaN/GaN nanocolumn LEDs emitting from blue to red *Proc. SPIE* **6473**

[6] Lin H-W, Lu Y-J, Chen H-Y, Lee H-M and Gwo S 2010 InGaN/GaN nanorod array white light-emitting diode *Appl. Phys. Lett.* **97** 073101

[7] Bavencove A-L *et al* 2011 Light emitting diodes based on GaN core/shell wires grown by MOVPE on n-type Si substrate *Electron. Lett.* **47** 765–7

[8] Johansson J and Dick K A 2011 Recent advances in semiconductor nanowire heterostructures *CrystEngComm* **13** 7175–84

[9] Tomioka K, Tanaka T, Hara S, Hiruma K and Fukui T 2011 III-V Nanowires on Si substrate: selective-area growth and device applications, selected topics in quantum electronics *IEEE J. Sel. Top. Quantum Electron.* **17** 1112–29

[10] Tomioka K, Yoshimura M and Fukui T 2012 A III-V nanowire channel on silicon for high-performance vertical transistors *Nature* **488** 189–92

[11] Saxena D, Mokkapati S, Parkinson P, Jiang N, Gao Q, Tan H H and Jagadish C 2013 Optically pumped room-temperature GaAs nanowire lasers *Nat. Photonics* **7** 963–8

[12] Mandl M *et al* 2013 Group III nitride coreshell nano- and microrods for optoelectronic applications *Phys. Status Solidi (RRL)* **7** 800–14

[13] Wang X, Jahn U, Mandl M, Schimpke T, Hartmann J, Ledig J, Straßburg M, Wehmann H-H and Waag A 2015 Growth and characterization of mixed polar GaN columns and coreshell LEDs *Phys. Status Solidi* A **212** 727–31

[14] Schimpke T *et al* 2016 Phosphor-converted white light from blue-emitting InGaN microrod LEDs *Phys. Status Solidi* A 1–8

[15] Kuykendall T, Ulrich P, Aloni S and Yang P 2007 Complete composition tunability of InGaN nanowires using a combinatorial approach *Nat. Mater.* **6** 951–6

[16] Li S and Waag A 2012 GaN based nanorods for solid state lighting *J. Appl. Phys.* **111**

[17] Robinson I and Harder R 2009 Coherent x-ray diffraction imaging of strain at the nanoscale *Nat. Mater.* **8** 291–8

[18] Dubslaff M, Hanke M, Burghammer M, Schöder S, Hoppe R, Schroer C G, Mazur Yu I, Wang Zh M, Lee J H and Salamo G J 2011 In(Ga)As/GaAs(001) quantum dot molecules probed by nanofocus high resolution x-ray diffraction with 100 nm resolution *Appl. Phys. Lett.* **98**

[19] Gulden J, Mariager S O, Mancuso A P, Yefanov O M, Baltser J, Krogstrup P, Patommel J, Burghammer M, Feidenhans'l R and Vartanyants I A 2011 Coherent x-ray nanodiffraction on single GaAs nanowires *Phys. Status Solidi* A **208** 2495–8

[20] Keplinger M, Grifone R, Greil J, Kriegner D, Persson J, Lugstein A, Schülli T and Stangl J 2016 Strain distribution in single, suspended germanium nanowires studied using nanofocused x-rays *Nanotechnology* **27** 055705

[21] Hanke M, Dubslaff M, Schmidbauer M, Boeck T, Schöder S, Burghammer M, Riekel C, Patommel J and Schroer C G 2008 Scanning x-ray diffraction with 200 nm spatial resolution *Appl. Phys. Lett.* **92** 193109

[22] Biermanns A, Carbone D, Breuer S, Jacques V L R, Schülli T, Geelhaar L and Pietsch U 2013 Distribution of zinc-blende twins and wurtzite segments in GaAs nanowires probed by x-ray nanodiffraction *Phys. Status Solidi (RRL)* **7** 860–3

[23] Etzelstorfer T *et al* 2014 Scanning x-ray strain microscopy of inhomogeneously strained Ge micro-bridges *J. Synchrotron Radiat.* **21** 111–8

[24] Stankevič T *et al* 2015 Fast strain mapping of nanowire light-emitting diodes using nanofocused x-ray beams *ACS Nano* **9** 6978–84

[25] Bussone G, Schäfer-Eberwein H, Dimakis E, Biermanns A, Carbone D, Tahraoui A, Geelhaar L, Bolívar P H, Schülli T U and Pietsch U 2015 Correlation of electrical and structural properties of single as-grown GaAs nanowires on Si (111) substrates *Nano Lett.* **15** 981–9

[26] Wang X *et al* 2013 Continuous-Flow MOVPE of Ga-polar GaN column arrays and core/shell led structures *Cryst. Growth Des.* **13** 3475–80

[27] Niehle M and Trampert A 2015 Electron tomography on nanopores embedded in epitaxial GaSb thin films *Micron* **73** 54–62

[28] Schroer C G *et al* 2005 *Appl. Phys. Lett.* **87** 124103

[29] Hirth J P and Lothe J 1991 *Theory of Dislocations* (New York: Wiley)

[30] Shimada K 2006 First-principles determination of piezoelectric stress and strain constants of wurtzite III nitrides *Japan. J. Appl. Phys.* **45** L358

[31] Als-Nielsen J and McMorrow D 2010 *Elements of Modern X-Ray Physics* (Chichester: Wiley)

[32] Stangl J, Mocuta C, Chamard V and Carbone D 2013 *Nanobeam x-ray Scattering* (Weinheim: Wiley)

[33] Dubslaff M, Hanke M, Patommel J, Hoppe R, Schroer C G, Schöder S and Burghammer M 2012 Scanning x-ray nanodiffraction: from the experimental approach towards spatially resolved scattering simulations *Nanoscale Res. Lett.* **7** 1–8

[34] Li Q and Wang G T 2010 Spatial distribution of defect luminescence in GaN nanowires *Nano Lett.* **10** 1554–8